DOI: 10.1002/chem.200800172

Photoluminescent Microporous Lanthanide Silicate AV-21 Frameworks

Collin M. Kowalchuk,[a] Filipe A. A. Paz,[a] Duarte Ananias,[a] Philip Pattison,[c] Luís D. Carlos,[b] and João Rocha*[a]

Abstract: The hydrothermal synthesis and structural characterization of the lanthanide silicate system $[Na_6Ln_2Si_{12}O_{30}{\cdot}x\,H_2O]$ ($Ln = La^{3+}$, Sm^{3+}, Eu^{3+}, Gd^{3+}, and Tb^{3+}), named AV-21, has been reported. Structural elucidation of the Sm^{3+} analogue (isomorphous with the Eu^{3+}, Gd^{3+}, and Tb^{3+} frameworks) using single-crystal synchrotron X-ray diffraction and solid-state NMR spectroscopy reveal disorder in the Si(1) second coordination sphere. La-AV-21 presents a distinct framework. These materials combine microporosity and interesting photoluminescence features with structural flexibility that allows the introduction of a second or third type of lanthanide center. Room-temperature lifetime decay dynamics have been used to estimate the Ln^{3+}–Ln^{3+} distances and the maximum distance over which energy transfer is active. Though the majority of Ln^{3+} centers occupy regular framework positions, the Ln(2) defect centers are disordered over the Na(1) sites in the pores and greatly influence the energy-transfer process, providing a unique opportunity for studying the relationship between structural disorder and photoluminescence properties in framework solids.

Keywords: hydrothermal synthesis · lanthanides · luminescence · microporous materials · silicates

Introduction

Zeolites are crystalline, hydrated aluminosilicates with open three-dimensional structures built of $[SiO_4]^{4-}$ and $[AlO_4]^{5-}$ tetrahedra linked to form regular intracrystalline cavities and channels of molecular dimensions. These materials are of considerable technological importance as shape-selective catalysts, ion-exchange solids, and molecular sieves. At present, there is an interest in silicate materials with zeolite-type structures and containing stoichiometric amounts of metal atoms (Ti, Zr, V, Nb, Sn, etc.) in different coordination geometries.[1] Moreover, many other materials with zeolite-type structures, particularly porous aluminophosphates and derivatives, contain tetrahedrally coordinated metal atoms.[2]

Recently, microporous silicate materials have been reported that incorporate lanthanide (Ln) centers and possess interesting new structures and photoluminescence properties.[3–9] This research aims at designing new materials, which combine microporosity and photoluminescence, that is, the traditional properties associated with zeolites and phosphors. Previous work on Ln silicate AV-21,[10] showed that the structures of this and other materials[11,12] are related to the structure of the mineral sazhinite.[13]

Lanthanide complexes exhibit great potential for photonic applications as light sources, X-ray phosphors and scintillator display devices, detector systems, light-emitting diodes, and solid state lasers.[14,15] Furthermore, lanthanide luminescent probes can be utilized to study the symmetry and the local environment in a variety of compounds.[15]

Herein, we present a detailed study of the structure and photoluminescence properties of the AV-21 system, $[Na_6Ln_2Si_{12}O_{30}{\cdot}x\,H_2O]$ ($Ln = La$, Sm^{3+}, Eu^{3+}, Gd^{3+}, and Tb^{3+}). Mixed lanthanide AV-21 samples, containing up to three types of Ln^{3+} ions, are reported for the first time. Because of the small crystal size (typically $0.01 \times 0.05 \times 0.05$ mm) and disorder in the Si(1) second coordination sphere, the structural characterization was not trivial and required the combination of single-crystal synchrotron X-ray

[a] Dr. C. M. Kowalchuk, Dr. F. A. A. Paz, Dr. D. Ananias, Prof. J. Rocha
Department of Chemistry, University of Aveiro
CICECO, 3810–193 Aveiro (Portugal)
Fax: (+351) 234-370-084
E-mail: rocha@ua.pt

[b] Prof. L. D. Carlos
Department of Physics, University of Aveiro
CICECO, 3810–193 Aveiro (Portugal)

[c] Prof. P. Pattison
European Synchrotron Research Facility
Swiss Norwegian Beam Line, 38043 Grenoble, Cedex (France)

Supporting information for this article is available on the WWW under http://www.chemeurj.org/ or from the author.

diffraction analysis (XRD) and solid-state NMR spectroscopy.

To rationalize the photoluminescence properties (except for the La compound), it was crucial to characterize the AV-21 structural disorder in detail. Indeed, while the ideal crystal structure calls for the presence of a unique Ln(1) ion, the "real" structure contains a second Ln(2) ion disordered over the Na(1) position in the micropores. XRD analysis, and NMR and photoluminescence spectroscopies suggest that the Ln(1)/Ln(2) population ratio of these two sites is about 5.24–5.56. The presence of Ln(2) ions disordered over the Na(1) sites activates the energy transfer, explaining certain features, such as low migration probabilities and good efficiencies. Thus, the present Ln silicate system offers a unique opportunity to discuss the relationship between structural disorder and optical properties in an extended framework (note that disorder in this system is possible due to the presence of micropores).

This paper is organized as follows: 1) We start by describing the single-crystal structure of Sm-AV-21, which is representative of this family of materials. Only crystals from this ion were suitable for full structure solution (although, due to the small $0.01\times0.05\times0.05$ mm size, we had to resort to data collected at the micro single crystal XRD facility at the ESRF in Grenoble). For the other materials, unit cell parameters could be extracted from single-crystal analysis. 2) The disorder in Sm-AV-21 is discussed in detail based on XRD and solid-state NMR data. 3) The second (not disordered) structural type, La-AV-21, is described. 4) The photoluminescence properties of selected single and mixed Ln samples are described in detail.

Table 1. Crystal and structure refinement data for Sm-AV-21 and La-AV-21.

	Sm-AV-21	La-AV-21
formula	$H_{9.76}Sm_{2.36}Na_{4.92}O_{34.88}Si_{12}$	$H_5LaNa_3O_{17.5}Si_6$
formula weight	1363.10	661.46
crystal system	orthorhombic	orthorhombic
space group	*P*mna	*C*mm2
a [Å]	7.5300(1)	7.4083(2)
b [Å]	7.0500(1)	30.9862(8)
c [Å]	14.9900(1)	7.1353(2)
volume [Å^3]	795.767(16)	1637.94(8)
Z	1	4
ρ_{calcd} [g cm^{-3}]	2.844	2.682
$\mu(Mo_{K\alpha})$ [mm^{-1}]	4.952	3.219
crystal size [mm]	$0.01\times0.05\times0.05$	$0.22\times0.08\times0.01$
crystal type	colorless plates	colorless plates
θ range	2.72 to 24.10	3.88 to 36.30
index ranges	$-8\le h\le 8$	$-11\le h\le 12$
	$-8\le k\le 8$	$-51\le k\le 51$
	$-16\le l\le 16$	$-11\le l\le 11$
reflections collected	3371	4252
independent reflections	683 ($R_{int}=0.0557$)	4252 ($R_{int}=0.0408$)
completeness	to $\theta=24.10°$, 99.1%	to $\theta=36.30°$, 99.6%
final *R* indices	$R1=0.0520$	$R1=0.0311$
$[I>2\sigma(I)]$[a,b]	$wR2=0.1349$	$wR2=0.0762$
final R indices	$R1=0.0711$	$R1=0.0324$
(all data)[a,b]	$wR2=0.1421$	$wR2=0.0766$
largest diff. peak and hole [eÅ^{-3}]	1.121 and −1.437	2.429 and −1.438

[a] $R1=\Sigma\,||F_0|-|F_c||/\Sigma\,|F_0|$. [b] $wR2=\sqrt{\sum[w(F_0^2-F_c^2)^2]/\sum[w(F_0^2)^2]}$.

Results and Discussion

Single-crystal structure of Sm-AV-21: The structure of the Sm-AV-21 phyllosilicate was solved from (micro)single-crystal X-ray diffraction data collected at the Swiss-Norwegian BM01a beamline at the ESRF (France, Grenoble), and the material can be formulated as $Na_4(Na_{0.92}Sm_{0.36})[Sm_2Si_{12}O_{30}]\cdot4.88\,H_2O$.

The crystal structure (orthorhombic *P*mna space group, Table 1) possesses two crystallographically independent silicon centers, Si(1) and Si(2) (rates of occupancy are 2:1, respectively), which constitute the basic building tetrahedra of a wollastonite-like silicate chain running parallel to the [100] crystallographic direction (Figure 1a). Adjacent chains coalesce through the μ_2-O(3) atom, imposing a Si(1)-O(3)-Si(1)^{ix} angle of 134.3(7)° and a Si(1)···Si(1)^{ix} distance of 2.994(2) Å, which lead to the formation of a corrugated chain composed of five-membered Si rings (Figure 1a; symmetry code: ix: $^1/_2-x$, y, $^1/_2-z$). These chains are further interconnected by the μ_2-O(5) atom, leading to eight-membered Si rings and ultimately the undulated anionic $[Si_2O_5^{2-}]_8$ layer extended in the *ac* plane of the unit cell (Figure 1b). It is of considerable importance to emphasize that the Si(2)–O(5)–Si(2)^{iv} linkage which forms these layers is linear (symmetry code: iv: $1-x$, $1-y$, $-z$), a feature attributed to the extensive structural disorder inherent to this family. Indeed, when compared with the remaining O atoms composing the framework, O(5) has larger thermal elliptical vectorial components (Figure 1c) similar to that observed for the Nd-based silicate materials reported by Haile and Wuensch.[12]

Adjacent anionic $[Si_2O_5^{2-}]_8$ layers are interconnected along the [010] direction of the unit cell by Sm(1) {SmO_6} octahedra (Figure 2a), forming a three-dimensional anionic framework (Figure 3) that shares striking similarities with the mineral sazhinite,[13] its lanthanum analogue,[16] a recently prepared Ce silicate,[11] and the α- and β- forms of a Nd silicate.[12] The structural stress imposed in the anionic $[Si_2O_5^{2-}]_8$ layers (see below for additional details) leads to a distorted octahedral coordination environment for Sm(1) as emphasized in Figure 2a, with the calculated Sm–O bond lengths and the *cis* O-Sm-O bond angles (Table 2) in the 2.303(8)–2.366(17) Å and 79.9(4)–97.6(3)° ranges, respectively. The distortion of the Sm(1) octahedron arises from the *cis* angles that deviate from the ideal. Indeed, as clearly depicted in Figure 2a, the magnitude of the vectorial components of thermal ellipsoid of atom O(6) are significantly larger than those of O(1), which is a further indication that the crystallographic position of the Si(2) tetrahedron (Figure 1c) varies slightly throughout the entire crystal volume.

Even though the two crystallographically independent SiO_4 tetrahedra that compose the undulated anionic $[Si_2O_5^{2-}]_8$ layer were refined with identical average Si–O

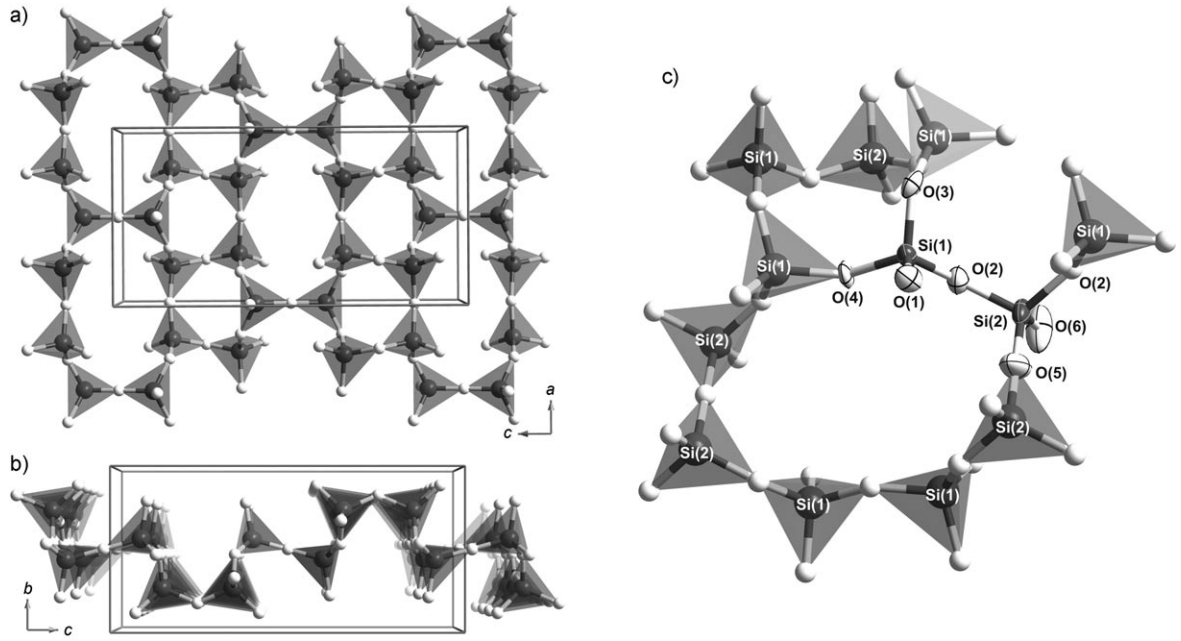

Figure 1. Undulated anionic $[Si_2O_5^{2-}]_8$ layer viewed in the perspective along the (a) [010] and (b) [100] directions of the unit cell. (c) A portion of the layer emphasizing the two crystallographically independent SiO_4 tetrahedra. Thermal ellipsoids are drawn at the 50% probability level, and atom labels (in black) are provided for all of the atoms belonging to the asymmetric unit of Sm-AV-21. Symmetry codes associated with the transformations used to generate equivalent atoms have been omitted for clarity. For selected bond lengths [Å] and angles [°] see Table 2.

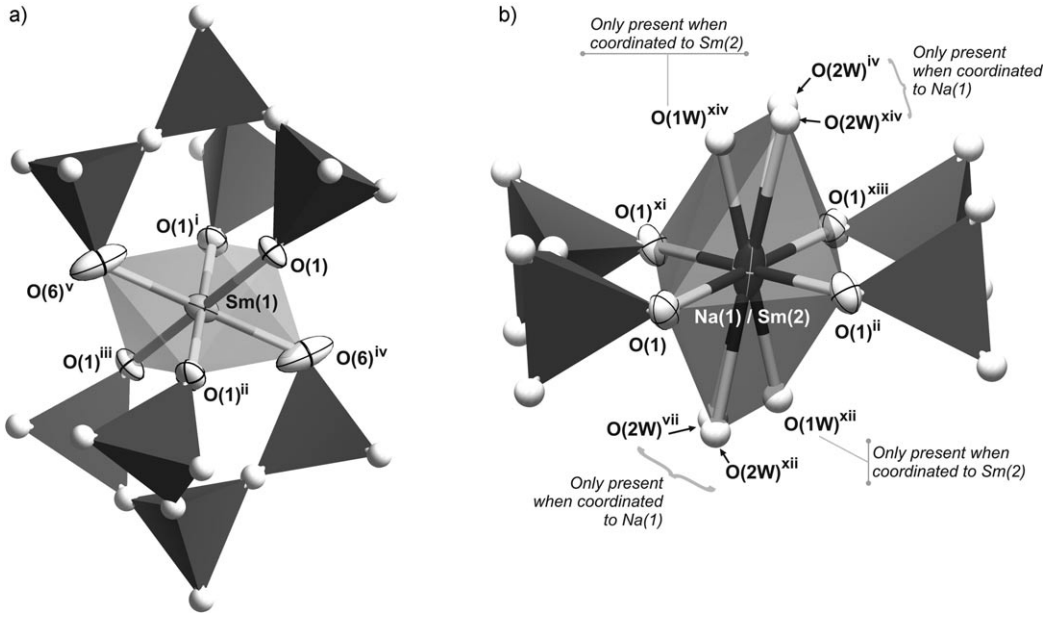

Figure 2. Schematic representation of the highly distorted octahedral $\{SmO_6\}$ coordination environments for a) Sm(1) and b) the disordered Na(1)/Sm(2) center located within the undulated anionic $[Si_2O_5^{2-}]_8$ layer. Atoms belonging to the first coordination sphere are represented with thermal ellipsoids drawn at the 50% probability level (except for the water molecules which have been refined by using isotropic displacement parameters). For selected bond lengths [Å] and angles [°] see Table 2. Symmetry transformations used to generate equivalent atoms: i: $1-x, y, z$; ii: $x, -y, -z$; iii: $1-x, -y, -z$; iv: $1-x, 1-y, -z$; v: $x, -1+y, z$; vii: $1-x, -1+y, z$; xi: $-x, y, z$; xii: $-1+x, -1+y, z$; xiii: $-x, -y, -z$; xiv: $-1-x, 1-y, -z$.

bond lengths (1.61(1) and 1.61(2) Å for Si(1) and Si(2), respectively; see Table 2), the second neighbors of these primary building units are markedly distinct, as ascertained by solid-state NMR spectroscopy (see below): the Si(2) tetrahedron interacts directly with Sm(1) and Na(2) (Sm(1)−O(6)^{iv} 2.366(17) Å; Na(2)···O(6) 2.31(2) Å; symmetry code: (iv)

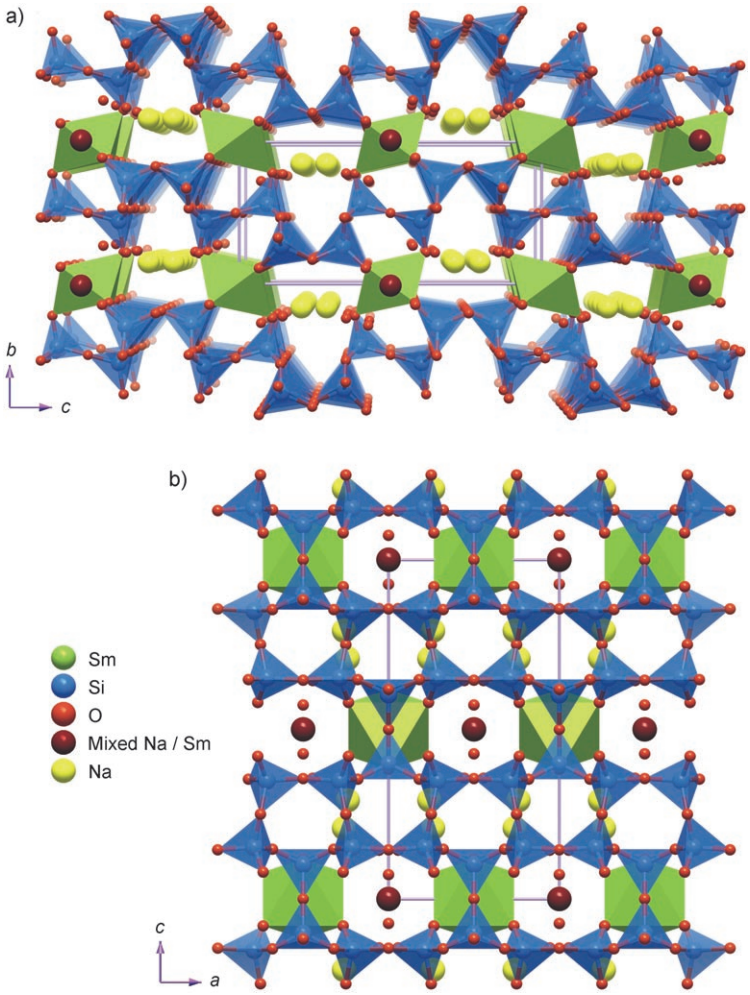

Figure 3. Crystal packing of Sm-AV-21 viewed in the perspective along the (a) [100] and (b) [010] crystallographic directions.

Table 2. Selected bond lengths [Å] and angles [°] for the SiO_4 tetrahedra and $\{SmO_6\}$ octahedra present in Sm-AV-21.[a]

Sm(1)–O(1)	2.303(8)	Si(1)–O(1)	1.551(8)
Sm(1)–O(6)^{iv}	2.366(17)	Si(1)–O(2)	1.605(8)
Sm(2)–O(1W)^{iv}	2.25(8)	Si(1)–O(3)	1.624(5)
Sm(2)–O(1)^{ii}	2.487(9)	Si(1)–O(4)	1.673(5)
Na(1)–O(2W)^{iv}	2.72(3)	Si(2)–O(2)	1.647(8)
		Si(2)–O(5)	1.586(6)
		Si(2)–O(6)	1.544(15)
O(1)^{i}-Sm(1)-O(1)^{ii}	180.0(3)	O(1)-Sm(2)-O(1)^{ii}	73.0(4)
O(6)^{iv} -Sm(1)-O(6)^{v}	180.0(8)	O(1)-Sm(2)-O(1)^{xi}	107.0(4)
O(1)^{i} -Sm(1)-O(1)	79.9(4)	O(1)-Sm(2)-O(1)^{xiii}	180.0(4)
O(1)^{ii} -Sm(1)-O(1)	100.1(4)	O(1W)^{iv} -Sm(2)-O(1)	86.4(14)
O(1)-Sm(1)-O(6)^{iv}	82.4(3)	O(1W)^{xii} -Sm(2)-O(1)	93.6(14)

[a] Symmetry transformations used to generate equivalent atoms: i: $1-x$, y, z; ii: x, $-y$, $-z$; iv: $1-x$, $1-y$, $-z$; v: x, $-1+y$, z; xi: $-x$, y, z; xiii: $-1+x$, $-1+y$, z; xiii: $-x$, $-y$, $-z$.

$1-x$, $1-y$, $-z$); Si(1) instead interacts with Sm(1) and Na(1) (Sm(1)–O(1) 2.301(8) Å; Na(1)···O(1)^{i} 2.487(9) Å; symmetry code: (ii) x, $-y$, $-z$). Moreover, the structural distinction between these SiO_4 tetrahedra arises primarily from the neighboring Na^+ centers, while Na(1) is structurally positioned within the corrugated anionic $[Si_2O_5^{2-}]_8$ layer (brown spheres in Figure 3), Na(2) is located within the structural cavities (Figure 3 - Na^+ represented in yellow).

Single-crystal unit cell measurements provide additional evidence that very similar frameworks arise from the isomorphous substitution of alternate lanthanide combinations (Table 3). Moreover, powder X-ray diffraction data of the bulk materials collected at ambient temperatures display similar features for all studied materials (see Supporting Information).

Disorder in Sm-AV-21: High-resolution single-crystal X-ray analysis shows that the crystallographic position of Na(1) is also shared with a partially occupied Sm(2) center (Figure 2b). This statistical disorder is not unprecedented among the members of this structural family. Moreover, Tsapatsis and co-workers postulated that the presence of an unknown ratio of compensating Ce^{3+} and Ce^{4+} centers for the Ce-containing material could explain this apparent discrepancy in overall crystal charge.[11] Furthermore, from a pure geometrical per-

Table 3. Unit cell metrics for synthesized AV-21 materials.

AV-21 material	a [Å]	b [Å]	c [Å]	V [Å^3]	Crystal system/ Bravais lattice
Sm[a]	7.5300(1)	7.0500(1)	14.9900(1)	795.77	orthorhombic P
Eu	7.118	7.349	15.26	798.25	orthorhombic P
Eu(0.78) Tb(0.22)	7.083	7.291	15.199	775.11	orthorhombic P
Eu(0.57) Tb(0.43)	7.01	7.25	15.04	764.37	orthorhombic P
Eu(0.39) Tb(0.61)	7.10	7.34	15.22	793.17	orthorhombic P
Eu(0.20) Tb(0.80)[a]	7.1231(3)	7.3561(5)	15.2160(7)	797.29	orthorhombic P
Tb	7.0781(19)	7.341(2)	15.132(4)	786.26	orthorhombic P
Eu(0.19) Gd(0.81)	7.09	7.32	15.23	790.42	orthorhombic P
Tb(0.25) Gd(0.75)	7.11	7.35	15.19	793.81	orthorhombic P

[a] Unit cell parameters collected from (micro)single crystal X-ray diffraction data collected at the BM01a beam line at the ESRF.

spective, this statistical structural disorder is greatly facilitated by minimal framework strain due to size similarity between the cationic radii of Ln^{3+} and Na^{+}.[17] Also, Thorpe and co-workers recently demonstrated that silicate networks, in particular zeo-type materials, are not rigid and can accommodate a number of different framework densities.[18] The structural diversity associated with the undulated anionic $[Si_2O_5^{2-}]_8$ layer is a striking example of such flexibility.

Remarkably, the highly distorted pseudo-octahedral coordination environment of the mixed Na(1)/Sm(2) site is distinct for each type of cation, even though the equatorial plane is always composed of four O(1) arising from four symmetry-related Si(1) tetrahedra. For Na(1) the two apical positions are occupied by a disordered O(2W) from a water molecule (Na(1)···O(2W) is 2.72(3) Å), whereas for Sm(2), they are instead occupied by O(1W) (Sm(2)–O(1W) is 2.25(8) Å; Figure 2b). For Sm(2), the *cis* O-Sm-O bond angles were found in the 73.0(4)–107.0(4)° range, with both the maximum and minimum values arising from the rigid geometry imposed on the equatorial plane by the two adjacent anionic $[Si_2O_5^{2-}]_8$ layers. The presence of this extra SmO_6 octahedron due to the partially occupied Sm(2) leads to the formation of a one-dimensional chain (running parallel to the [100] crystallographic direction) of optical centers with the shortest Sm(1)···Sm(2) and Sm(2)···Sm(2)^{vi} distances being 3.765(1) and 7.050(1) Å, respectively (symmetry code: vi: $1+x, y, z$; see the Supporting Information).

It is also interesting to note that the structural disorder associated with the partial occupancies of the Na(1)/Sm(2) pair seems to further introduce short- and long-range framework disorder due to the presence of vacancies within the material. Indeed, whereas the idealized AV-21 stoichiometry requires the occupation of 2 Na(1) to Na(2) centers within each unit cell, the refined stoichiometric formula for Sm-AV-21 results from an 18% replacement of Na(1) by Sm(2) cations. Since each Sm^{3+} ion effectively replaces three Na^{+} ions, the framework contains 36% empty coordination sites for the crystallographic position of the Na(1)/Sm(2) pair. Consequently, it is feasible to assume that the combined effect of the presence of highly charged cations and/or vacancies leads to structural distortions in its surroundings.

The ^{29}Si magic-angle spinning (MAS) NMR spectrum of Sm-AV-21 (Figure 4) displays three resonances. The spectra of samples produced in different syntheses are similar to this spectrum. Thus, ^{29}Si MAS NMR spectroscopy supports the refined (rather than the ideal) crystal structure, which reveals the presence of disorder in the Si(1) second coordination sphere. Moreover, Si(1) is coordinated to O(1), which is linked to a Sm(1) but may also coordinate to a partially occupied Na(1) or Sm(2), thus generating three different chemical environments (besides the Si(2) site): Si(1)[3Si,Sm(1)], Si(1)[3Si,Sm(1),Na(1)], and Si(1)-[3Si,Sm(1),Sm(2)]. Because of the paramagnetism of Sm^{3+}, the peak at $\delta = -114.3$ ppm is assigned to the latter site. The resonance at $\delta = -101.2$ ppm is attributed to Si(1)[3Si,Sm(1)], whereas the peak at $\delta = -106.3$ contains contributions from both the Si(1)[3Si, Sm(1), Na(1)] and Si(2)[3Si, Sm(1), Na(2)] environments. The ^{29}Si MAS NMR spectrum may be simulated by assuming the populations given in Table 4 and derived from XRD evidence.

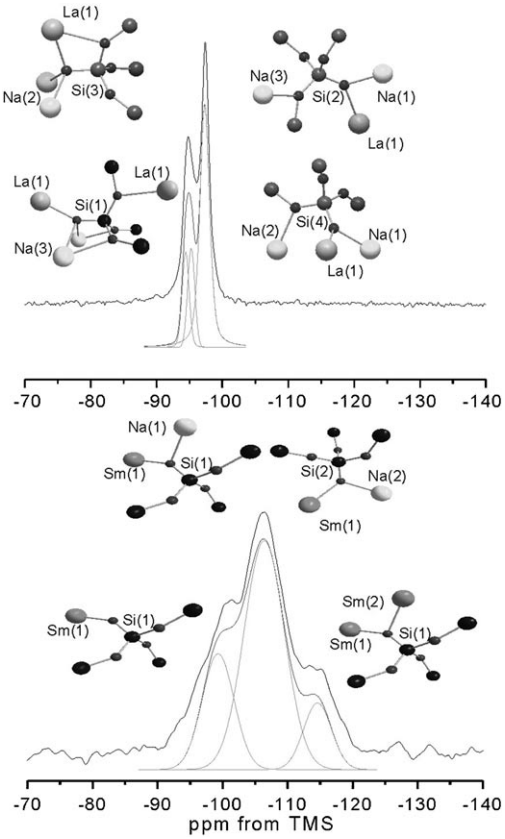

Figure 4. ^{29}Si MAS NMR spectra: Sm-AV-21 (bottom), simulated with an 18% substitution of Sm(2) for Na(1) and La-AV-21 (top).

Table 4. Simulated data from the ^{29}Si MAS NMR spectrum of Sm-AV-21.

Peak [ppm]	Si environments	Gaussian peak area	Si populations
−101.2	Si(1) [3Si,Sm(1)]	0.40	0.36
−106.3	Si(1)[3Si,Sm(1),Na(1)] + Si(2)[3Si, Sm(1),Na(2)]	1.00	0.46 + 0.5
−114.3	Si(1)[3Si,Sm(1),Sm(2)]	0.20	0.18

The ^{23}Na triple-quantum (3Q) MAS NMR spectrum of Sm-AV-21 reveals the presence of two resonances (Figure 5). The single quantum ("conventional") MAS NMR spectrum may be simulated by assuming a 1:4.5 Na(1):Na(2) population ratio derived from the refined crystal model (Figure 5, top).

Structure of La-AV-21: The use of La^{3+} ions in the synthesis gel led to a different material composed of very thin plates and has the formula, $Na_3[LaSi_6O_{15}]\cdot 2.5\,H_2O$ (La-AV-21), on the basis of single-crystal X-ray diffraction data (Table 1).

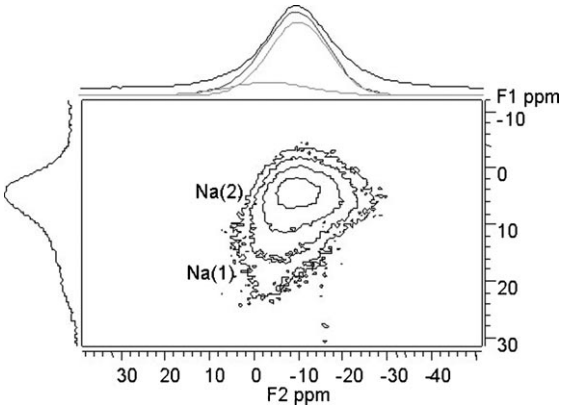

Figure 5. Triple-quantum ^{23}Na MAS NMR spectrum of Sm-AV-21 reveals two ^{23}Na resonances. The ^{23}Na MAS spectrum of Sm-AV-21 (top) was simulated with the 1:4.5 ratio of Na(1):Na(2).

The La-AV-21 material contains a single crystallographically independent La^{3+} center that exhibits a LaO_7 coordination sphere resembling a highly distorted capped trigonal prism (Figure 6b). This highly distorted coordination sphere arises from edge-sharing between the La^{3+} polyhedron and the Si(3) tetrahedron, leading to a coordination geometry intermediate between an octahedron and a pentagonal bipyramid. This structural feature is ultimately reflected in the large range for the La–O bond lengths (2.361(3)–2.735(3) Å) and in some internal O-La-O polyhedral angles, which are reminiscent of those of an octahedron (i.e. those involving the O(1), O(3), and O(11) atoms), whereas others deviate (i.e. those involving the O(8) and O(9) atoms and composing the shared edge; Figure 6c and Table 5). As for the Sm-AV-21 material previously described, the La(1) centers interconnect adjacent anionic $[Si_6O_{15}^{6-}]_8$ layers along the [100] direction of the unit cell. This leads to a porous three-dimensional anionic framework having two types of eight-membered ring channels (parallel to the *a* axis), which contain the charge-balancing Na^+ ions and three crystallographically independent water molecules (Figure 6c). The closest intermetallic La(1)···La(1)^{v} distance, 7.1353(5) Å (symmetry code: v: x, y, $-1+z$), occurs between consecutive centers across anionic $[Si_6O_{15}^{6-}]_8$ layers.

We note that the structural features of the La-AV-21 framework are similar to the material $Na_{2.4}CeSi_6O_{15}{\cdot}2.6\,H_2O$ recently reported by Yu and co-workers.[19] However, in La-AV-21 the lanthanide center accommodates only one oxidation state, hence the different number of Na^+ ions located within the pores of the framework. La-AV-21 contains four crystallographically independent Si centers, two half-occupied in the asymmetric unit (Si(1) and Si(3)) and another two with full-site occupancy (Si(2) and Si(4)). As previously described for Sm-AV-21, the tetrahedral nodes are also interconnected into wollastonite-like silicate chains running parallel to the [100] crystallographic direction (Figure 6a). The coalescence of neighboring chains is, however, different, leading to a distinct anionic $[Si_6O_{15}^{6-}]_8$ layer (Figure 6a). On the one hand, half of the chains are joined together as in the Sm-AV-21 material, leading to corrugated chains composed of alternating five-membered Si rings, and on the other, the remaining half coalesce in such a way that a chain composed of alternating four- and five-membered rings are formed instead. It is of considerable importance to emphasize that this decrease in the symmetry of the $[Si_6O_{15}^{6-}]_8$ layers is accompanied crystallographically by a duplication of the corresponding unit cell axis (see Table 1).

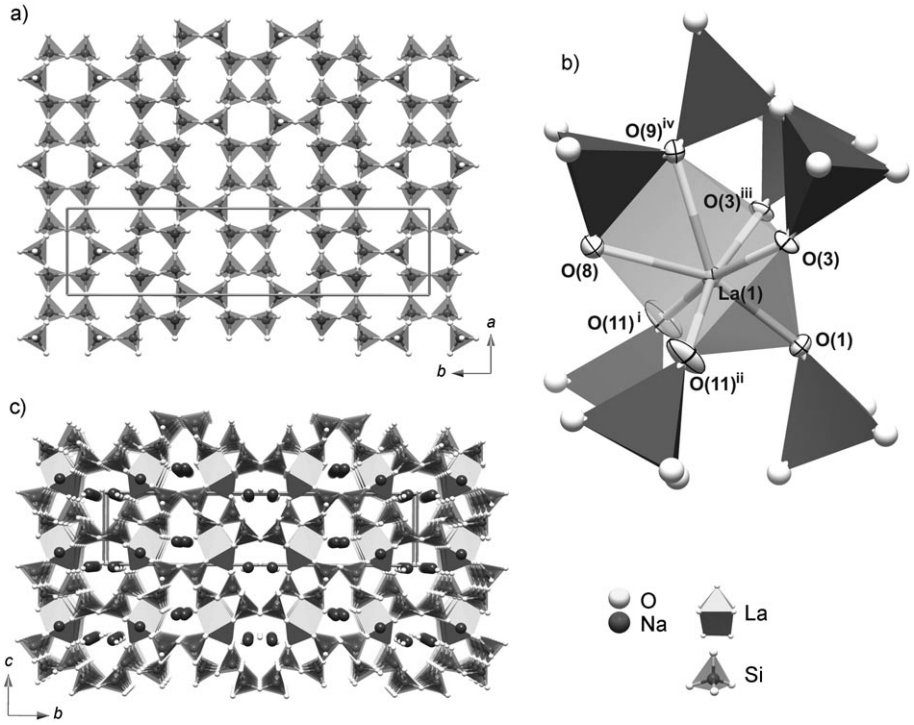

Figure 6. a) Undulated anionic $[Si_6O_{15}^{6-}]_8$ layer viewed in the perspective along the [001] direction of the unit cell. b) Schematic representation of the highly distorted pseudo-octahedral $\{LaO_7\}$ coordination environment present in La-AV-21. Thermal ellipsoids are drawn at the 80% probability level and atom labels (in black) are provided for all the atoms belonging to the first coordination sphere. For selected bond lengths [Å] and angles [°] see Table 5. c) Crystal packing of La-AV-21 viewed in the perspective along the [100] crystallographic direction.

Table 5. Selected bond lengths [Å] and angles [°] for the {LaO_7} polyhedron present in La-AV-21.[a]

La(1)–O(1)	2.361(3)	La(1)–O(9)^{iv}	2.735(3)
La(1)–O(3)	2.450(2)	La(1)–O(11)^{i}	2.408(3)
La(1)–O(8)	2.554(4)		
O(1)-La(1)-O(3)	81.81(8)	O(8)-La(1)-O(9)^{iv}	57.74(11)
O(1)-La(1)-O(8)	156.92(12)	O(11)^{i}-La(1)-O(3)	166.91(10)
O(1)-La(1)-O(9)^{iv}	145.34(11)	O(11)^{ii}-La(1)-O(3)	78.31(9)
O(1)-La(1)-O(11)^{i}	85.78(10)	O(11)^{i}-La(1)-O(8)	80.25(10)
O(3)-La(1)-O(3)^{iii}	95.73(11)	O(11)^{i}-La(1)-O(9)^{iv}	113.84(9)
O(3)-La(1)-O(8)	112.84(8)	O(11)^{i}-La(1)-O(11)^{ii}	104.99(14)
O(3)-La(1)-O(9)^{iv}	75.19(7)		

[a] Symmetry transformations used to generate equivalent atoms: i: x, $-y$, $-z$; ii: $1-x$, y, z; iii: $1-x$, $-y$, $-z$; iv: $1-x$, $1-y$, $-z$.

The ^{29}Si MAS NMR spectrum of La-AV-21 (Figure 4) displays two relatively sharp peaks at $\delta = -94.7$ and -97.4 ppm. The crystal structure calls for four distinct Si sites of the types Si [2Si] (for Si(2) and Si(4)) and Si [3Si] (for Si(1) and Si(3)) and, thus, two main resonances are expected. Note, however, that the full second coordination spheres of Si(1) and Si(3) are different and, indeed, we found that a good deconvolution of the spectrum requires two peaks at $\delta = -94.4$ and -95.2 ppm and not just one.

Optical properties: photoluminescence spectroscopy study: *Excitation and emission spectra*: Here we will discuss the photoluminescence properties of the [$Na_6Ln_2Si_{12}O_{30}{\cdot}x\,H_2O$] (Ln = Eu^{3+}, Gd^{3+}, and Tb^{3+}) system. The crystal structure of Sm-AV-21 and the nature of its disorder will be used as a reference because these features are not available for the materials with other lanthanides. The Eu-AV-21 room-temperature excitation spectrum, monitored at 610.0 nm displays sharp lines ascribed to intra-4f^6 transitions between the $^7F_{0-2}\rightarrow{}^5D_{4-0}$, $^5L_6$, and ^5G_J ($2 \le J \le 6$) Eu^{3+} states (Figure 7). The low temperature (40 K) excitation spectrum is similar (not shown), except for the absence of the $^7F_1\rightarrow{}^5D_3$ and $^7F_{1,2}\rightarrow{}^5D_1$ transitions. Although sharp excitation transitions were also observed from Tb^{3+} centers in AV-21 when monitored at 540.0 nm ($^5D_4\rightarrow{}^7F_5$), broad bands between 225 and 300 nm dominate the spectrum (Figure 7). The sharp lines are assigned to $^7F_6\rightarrow{}^5D_{4-0}$, $^5L_{10}$, and $^5G_{6-3}$ $4f^8\rightarrow 4f^8$ Tb^{3+} transitions. The bands at about 257 nm are attributed to spin forbidden (high spin, HS) interconfigurational $4f^8\rightarrow 4f^75d^1$ Tb^{3+} transitions arising for lanthanide ions with more than seven 4f electrons.[5,21–23] Higher energy spin allowed (low spin, LS) fd transitions[21,22] are observed at about 241 nm for the Eu^{3+} and Tb^{3+} analogues. Because spectral correction was not performed below 240 nm, the LS and HS band intensities may not be compared.

The room-temperature emission spectrum of Eu-AV-21 excited at 392.0 nm displays sharp lines assigned to the transitions between the first excited non-degenerate $^5D_0$ state and the $^7F_{0-4}$ levels of the fundamental Eu^{3+} septet (Figure 8). Luminescence from the higher $^5D_1$ excited state was not detected. Because only one $^5D_0\rightarrow{}^7F_0$ line is observed, the emission spectra do not provide direct evidence for the presence of two Eu^{3+} sites in AV-21. Additionally,

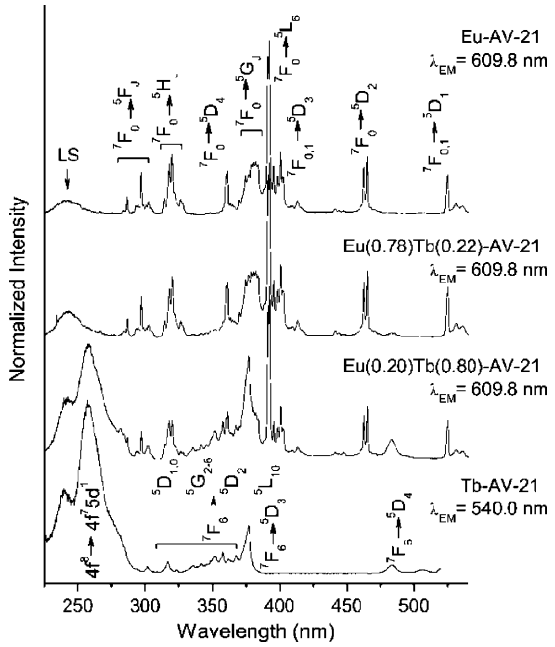

Figure 7. Excitation spectra of AV-21 materials.

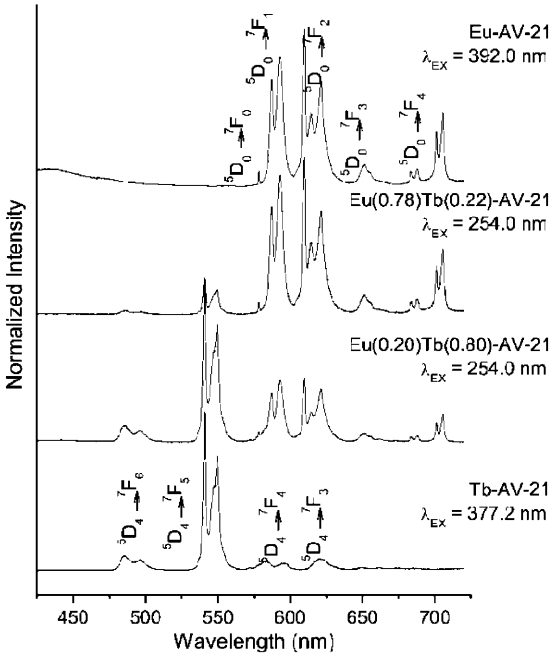

Figure 8. Emission spectra of AV-21 materials.

two Eu^{3+} local environments cannot be rationalized from the splitting of the $^5D_0\rightarrow{}^7F_1$ states. The similar distorted octahedral geometry about both Ln^{3+} centers could explain this observation. Low-temperature analysis of AV-21 cannot be performed without structural modification,[10] likely a result of a point symmetry modification about the Eu(2) centers due to dehydration. Direct evidence of two Eu^{3+} environments was, however, obtained from lifetime analysis of this sample (see below). The emission spectrum of Tb-AV-

21 excited at 377 nm displays strong $^5D_4 \rightarrow {}^7F_{3-6}$ lines and a weak $^5D_4 \rightarrow {}^7F_2$ transition (Figure 8). Luminescence from higher excited states was not detected. An advantageous property of Tb-AV-21 that may allow its use in diverse applications is the emission behavior when excited within the HS band ($\lambda = 254$ nm), an identical emission spectrum to that displayed in Figure 8 can be obtained. This broad band overlaps with the most intense line of the commercial Hg lamp.

Energy transfer: Biexponential decay curves suggest the presence of two Ln^{3+} environments, although, with judicious choice of experimental conditions, individual lifetime components can be isolated.[10] Long and short lifetimes were obtained ($R \geq 0.999$) from the decay curves of Eu- and Tb-AV-21 (Eu^{3+}: $\tau_1 = 2.989 \pm 0.005$ and $\tau_2 = 0.60 \pm 0.01$ ms, Tb^{3+}: $\tau_1 = 5.93 \pm 0.01$ and $\tau_2 = 1.15 \pm 0.03$ ms, see Supporting Information), a result that supports the presence of Ln^{3+} centers with and without coordinated H_2O.[6,7,21]

Energy transfers between long (7.1–7.3 Å) and short (3.8 Å) Ln–Ln distances, confined to two-dimensions were examined. It is well known that the energy transfer is predominantly multipolar between appropriate close contact donor/acceptor pairs,[21,22] which is consistent with the recently modelled energy migration within the AV-20 framework.[17] In the case of AV-21, no attempt was made to determine the overall energy transfer mechanism, instead an experimental examination of the energy migration characteristics was performed through extensive emission and lifetime studies. An investigation of Eu:Tb mixed frameworks with ratios of 0.78:0.22 and 0.20:0.80 (Eu(0.78)Tb(0.22)- and Eu(0.20)Tb(0.80)-AV-21, respectively) provides evidence for energy transfer within AV-21. The emission spectra of mixed EuTb-AV-21 demonstrate $Tb^{3+} \rightarrow Eu^{3+}$ energy transfer when excited at 254 nm within the Tb^{3+} HS band (Figure 8). Energy migration between Tb^{3+} and Eu^{3+} was verified from excitation spectra monitored at 609.8 nm within the $^5D_0 \rightarrow {}^7F_2$ band of Eu^{3+} (Figure 7).

The large intralayer Ln–Ln distances of 7.050(1) and 7.530(5) Å and an interlayer Ln–Ln spacing of 8.388(1) Å may hinder energy migration.[30,31] A simple operational definition of the $Tb^{3+} \rightarrow Eu^{3+}$ energy transfer probability in terms of lifetimes is given in Equation (1) .[25,26]

$$P_{Tb^{3+} \rightarrow Eu^{3+}} = \left(\frac{1}{\tau}\right) - \left(\frac{1}{\tau_0}\right) \quad (1)$$

Where τ and τ_0 are the Tb^{3+} donor lifetimes in the presence and absence of the Eu^{3+} acceptor, respectively. For the longer lifetime, probabilities of 0.072 (Eu(0.11)Tb(0.89)-AV-21) and 0.176 ms^{-1} (Eu(0.20)Tb(0.80)-AV-21) were obtained. These probabilities are much smaller than those reported for AV-22,[6] likely a result of the greater donor–acceptor separation. A typical energy transfer probability was calculated for Eu(0.78)Tb(0.22)-AV-21 ($P = 0.700$); however, the Eu:Tb ratio is much larger than normal for this type of calculation. Energy transfer efficiency values[25,26] of 0.30 and 0.51 were obtained from Eu(0.11)Tb(0.89)-AV-21 and Eu(0.20)Tb(0.80)-AV-21, respectively [Eq. (2)]

$$E_{Tb^{3+} \rightarrow Eu^{3+}} = \left(1 - \frac{\tau}{\tau_0}\right) \quad (2)$$

The Ln^{3+} ions in the Na(1) crystallographic position may activate the energy transfer and explain these low migration probabilities, but good efficiencies. Table 6 summarizes the lifetime data ($R \geq 0.999$) obtained from AV-21.

Table 6. Summary of the simulated second order lifetimes.

Framework (EDS ratios)	LT: Tb (ms) Ex: 377.2 nm Em: 540.9 nm	LT: Eu (ms) Ex: 392 nm Em: 609.8 nm
Eu(0.19)Gd(0.81)-AV-21	–	$\tau_1 = 3.266 \pm 0.008$
		$\tau_2 = 0.74 \pm 0.04$
Eu-AV-21	–	$\tau_1 = 2.989 \pm 0.005$
		$\tau_2 = 0.60 \pm 0.01$
Eu(0.92)Tb(0.08)-AV-21	$\tau_1 = 0.80 \pm 0.04$	$\tau_1 = 3.07 \pm 0.01$
	$\tau_2 = 0.36 \pm 0.02$	$\tau_2 = 0.59 \pm 0.02$
Eu(0.87)Tb(0.13)-AV-21	$\tau_1 = 1.18 \pm 0.08$	$\tau_1 = 3.088 \pm 0.007$
	$\tau_2 = 0.504 \pm 0.005$	$\tau_2 = 0.59 \pm 0.05$
Eu(0.78)Tb(0.22)-AV-21	$\tau_1 = 1.15 \pm 0.02$	$\tau_1 = 3.146 \pm 0.008$
	$\tau_2 = 0.574 \pm 0.003$	$\tau_2 = 0.59 \pm 0.03$
Eu(0.67)Tb(0.33)-AV-21	$\tau_1 = 1.21 \pm 0.03$	$\tau_1 = 3.199 \pm 0.003$
	$\tau_2 = 0.634 \pm 0.007$	$\tau_2 = 0.58 \pm 0.02$
Eu(0.57)Tb(0.43)-AV-21	$\tau_1 = 1.59 \pm 0.03$	$\tau_1 = 3.091 \pm 0.006$
	$\tau_2 = 0.755 \pm 0.006$	$\tau_2 = 0.58 \pm 0.03$
Eu(0.52)Tb(0.48)-AV-21	$\tau_1 = 1.60 \pm 0.03$	$\tau_1 = 3.165 \pm 0.006$
	$\tau_2 = 0.73 \pm 0.01$	$\tau_2 = 0.65 \pm 0.02$
Eu(0.39)Tb(0.61)-AV-21	$\tau_1 = 1.91 \pm 0.02$	$\tau_1 = 3.131 \pm 0.005$
	$\tau_2 = 0.807 \pm 0.009$	$\tau_2 = 0.57 \pm 0.02$
Eu(0.33)Tb(0.67)-AV-21	$\tau_1 = 2.35 \pm 0.01$	$\tau_1 = 3.237 \pm 0.007$
	$\tau_2 = 0.95 \pm 0.01$	$\tau_2 = 0.57 \pm 0.02$
Eu(0.20)Tb(0.80)-AV-21	$\tau_1 = 2.90 \pm 0.02$	$\tau_1 = 3.237 \pm 0.005$
	$\tau_2 = 1.10 \pm 0.02$	$\tau_2 = 0.61 \pm 0.02$
Tb-AV-21	$\tau_1 = 5.93 \pm 0.01$	–
	$\tau_2 = 1.15 \pm 0.03$	
Tb(0.25)Gd(0.75)-AV-21	$\tau_1 = 6.22 \pm 0.03$	–
	$\tau_2 = 2.66 \pm 0.12$	

The number (n) of Eu^{3+} centers capable of accepting energy transfer from Tb^{3+} ions may be estimated from Equation (3).[27]

$$\frac{I(Tb^{3+})}{I(\text{total})} = (1-\chi)^n \quad (3)$$

The integrated intensities of the donor $I(Tb^{3+})$ and I(total) were obtained from the emission spectra (Table 7) $(1-x)$ term, where x represents the acceptor ratio (Eu^{3+}) and incorporates the probability that a neighboring center of Tb^{3+} is not Eu^{3+}. An average value of $n = 2$ was obtained from the mixed EuTbGd-AV-21 samples and likely corresponds to dimensionally restricted energy transfer.[25] If energy migration is restricted to two dimensions within AV-21 by the insulating $[Si_2O_5^{2-}]_8$ layers, then the estimation of R_c, the

Table 7. Estimated number of Eu^{3+} centers (n) that can accept Tb^{3+} energy transfer.

EDS determined ratio of Tb/Eu/Gd	$I(Tb^{3+})/I$(total) (estimated error ±5%)	n
0.14/0.10/0.76	0.96	2 (1.57)
0.14/0.13/0.73	0.78	2 (1.78)
0.14/0.17/0.69	0.62	3 (3.03)

critical radius (the maximum Ln–Ln distance for energy transfer), can be calculated according to Equation (4).[27]

$$l = \left[\frac{\pi R_c^2}{n+1}\right]^{1/2} \quad (4)$$

The l variable represents the mean distance between Ln ions obtained from the XRD structure. If three-dimensional energy migration dominates, then the πR_c^2 term can be replaced by $4/3(\pi R_c)^3$. R_q, the maximum quenching Tb^{3+}–Eu^{3+} distance may be calculated in two-dimensions from Equation (5).[27]

$$R_q = \left[\frac{(n+1)l^2}{\pi}\right]^{1/2} \quad (5)$$

The low concentration of defect Ln(2) centers that occupy the Na(1) positions may significantly influence the energy migration. The Tb^{3+} biexponential decay curves (Figure 9) with different Eu:Tb ratios (Eu(x):Tb(1−x); $x=0$, 0.11, 0.20 and 0.78) demonstrate this with an efficient dynamic emission quenching by close proximity trap (Eu^{3+}) sites being observed.[28] Additional evidence for closely spaced Tb^{3+}–Eu^{3+} pairs (in Eu(0.06)Tb(0.94)-AV-21) was obtained from the decay curves of Eu^{3+} ($^5D_0$) when Tb^{3+} ($^5D_4$) was excited directly (see the Supporting Information); the classic Eu^{3+} energy build-up and subsequent non-exponential decay was observed.[5,30] Stern–Volmer plots of normalized Tb^{3+} lifetimes exhibit linear relationships over the entire Eu molar ratio range from both defect and regular framework positions (Figure 9, inset). This suggests that similar Eu(1):Eu(2) concentration ratios exist in all the Eu/Tb samples. Small deviations from linearity may be a result of slightly different Ln(1):Ln(2) ratios than those determined from the energy-dispersive spectrum (EDS). Since the Stern–Volmer kinetics usually only hold at small quencher concentrations,[29] τ_1 may be quenched by the closely spaced low concentration defect Eu(2) centers. Quencher concentrations derived from the Stern–Volmer plot[30] of $C(\tau_1)$ and $C(\tau_2)$ are $5.45{\cdot}x$ and $1.04{\cdot}x$ mol L^{-1}, respectively. Thus, the Eu(1):Eu(2) population ratio is 5.24, in fair agreement with the XRD ratio (5.56) obtained for Sm-AV-21. Moreover, the average EDS Si:Ln ratio of all Eu,Tb-AV-21 samples is 5.1. A general formula for these samples is, thus, $Na_4(Na_{0.95}Ln_{0.35})[Ln_2Si_{12}O_{30}]{\cdot}xH_2O$ (Ln = Eu, Tb), in which a similar partition of Eu and Tb over the framework and nonframework (defect) Ln sites is assumed. Because the Eu and Tb τ_1 lifetimes are larger than τ_2 (Table 6), the latter are attributed to non-framework sites, which have quenching OH oscillators (water molecules) in their first coordination sphere.

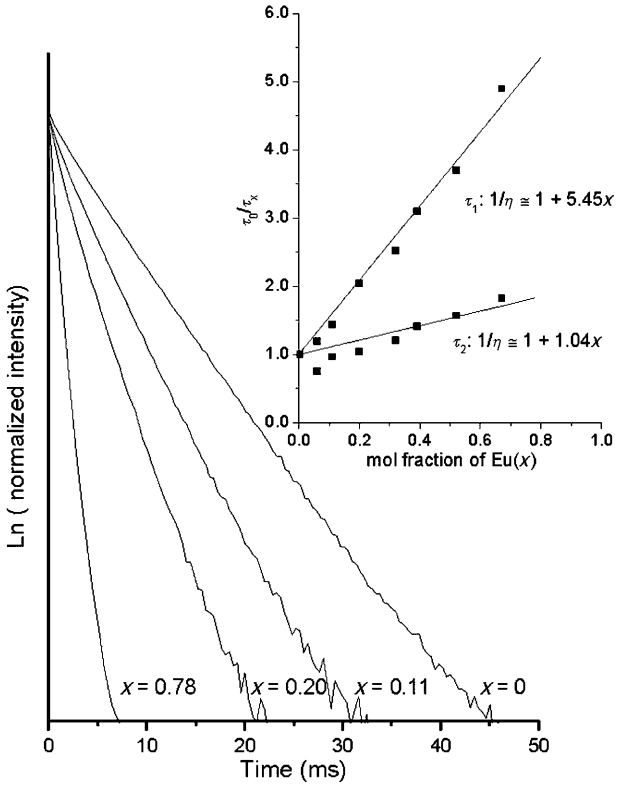

Figure 9. Tb^{3+} ($^5D_4$) decay curves of the Eu(x):Tb(1−x) ($x=0$, 0.11, 0.20 and 0.78) AV-21 samples. Inset, Stern–Volmer plots (ratio of lifetimes versus mole fraction of Eu(x)).

The longer lifetimes obtained for Eu(0.19)Gd(0.81)- and Tb(0.25)Gd(0.75)-AV-21 demonstrate that cross relaxation occurs within the framework (Table 6). Additional insight into energy migration may therefore be rationalized with respect to the presence of an energy scatter.[31] The decay curves of mixed EuTb(Gd)-AV-21 samples (Eu(1−x):Ln(x); Ln = Tb, Gd; $x=0$, ≈ 0.2) were only marginally affected (Figure 10) and linear relationships of Eu^{3+} lifetime (τ_1 and τ_2) versus the Eu molar ratio were obtained (Figure 10, inset). The plot of τ_1 versus the Eu mole ratio suggests inefficient energy migration. The τ_2 lifetime displays an independent relationship with respect to the Eu molar ratio (negligible energy migration); Eu(2) centers, therefore, exhibit the characteristics of a killer site.

Conclusion

The AV-21 lanthanide silicate system studied here provided a unique opportunity for investigating the relationship between structural disorder and photoluminescence in a microporous framework material. Disorder in the Sm analogue was comprehensively studied by single-crystal XRD and ^{29}Si and ^{23}Na solid-state NMR spectroscopy; the distribution of

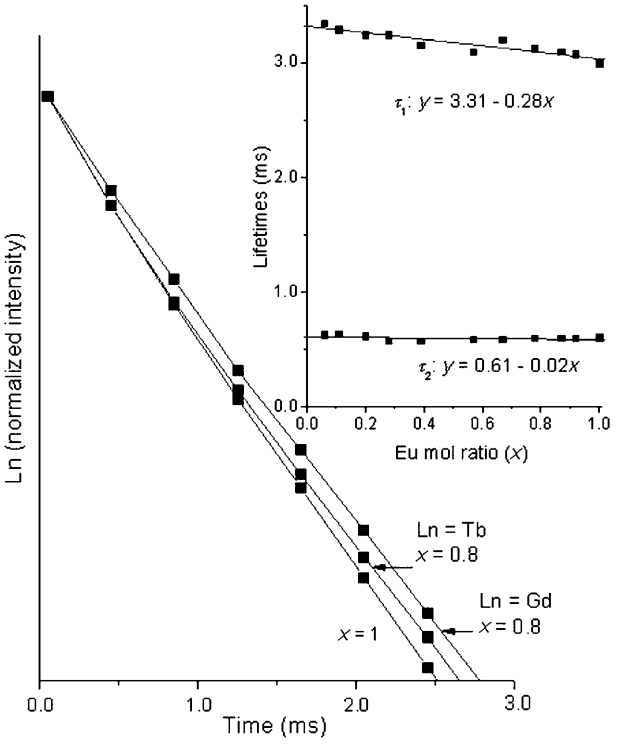

Figure 10. Eu^{3+} ($^5D_0$) decay curves of Eu(1−x):Ln(x) (x = 0, ≈0.20; Ln = Tb, Gd) samples that demonstrate the scattering effect. Inset, relationship between Eu^{3+} lifetimes and Eu^{3+}/Tb^{3+} mole ratio.

Eu^{3+} between the regular Eu(1) and defect Eu(2) sites in mixed Eu,Tb-AV-21 was derived from photoluminescence data (Stern–Volmer plots). The presence of micropores in the structure defines the nature of the disorder in the optically active sites: slightly less than one in five Ln^{3+} ions replace extra-framework Na^+ ions generating defect Ln(2) sites. Because the Ln(1)–Ln(2) distance is about 3.8 Å, much shorter than the minimum Ln(1)–Ln(1) distance (over 7 Å), the defect Ln(2) sites offer an efficient route for energy migration between optical centers. In short, rationalizing the photoluminescence properties of AV-21 materials requires a full understanding of their structural disorder, which is only gained by the tandem use of several structural characterization techniques.

Experimental Section

The preparation of the AV-21 (Ln = La, Sm, Eu, Tb, Eu/Tb, Eu/Gd and Tb/Gd) frameworks was carried out in Teflon-lined autoclaves (volume 42 cm^3, filling rate 70%), in ovens preheated to 230 °C under static hydrothermal conditions. Thoroughly mixed alkaline synthesis gels of the composition $1.18\,Na_2O{:}1.00\,SiO_2{:}0.037\,Ln_2O_3{:}42.4\,H_2O$, prepared from sodium silicate solution (7.28 g, 27% m/m SiO_2, 8% m/m Na_2O, Merck), H_2O (20.50 g), NaOH (0.82 g, Merck), NaCl (2.20 g, Panreac), and $LnCl_3{\cdot}6H_2O$ (2.41 mmol, Aldrich), were autoclaved for 7–14 days at 503 K. Large off-white crystals were isolated after the autoclaves were removed from the oven. These crystals were quenched with water, filtered, washed, and dried at 60 °C. Mixed Ln frameworks with Eu:Tb ratios of 0.92:0.08, 0.87:0.13, 0.78:0.22, 0.67:0.33, 0.57:0.43, 0.52:0.48, 0.39:0.61, 0.33:0.67, and 0.20:0.80, an Eu:Gd ratio of 0.19:0.81, a Tb:Gd ratio of 0.25:0.75, and Tb:Eu:Gd ratios of 0.14:0.10:0.76, 0.14:0.13:0.73, and 0.14:0.17:0.69, respectively, were prepared through the incorporation of the appropriate Ln concentrations into the synthesis gel. Extensive EDS analyses revealed that the mixed samples exhibited homogeneous lanthanide distributions both within individual and between different crystals.

A suitable (micro)single crystal ($0.01\times0.05\times0.05$ mm) of Sm-AV-21 was manually selected and mounted on a Hampton Research CryoLoop using PARATONE oil.[32] A complete single-crystal data set was collected at 100(2) K on a KUMA-KM6 goniometer at the Swiss-Norwegian BM01a beamline (ESRF, Grenoble, France), equipped with an Oxford Cryosystems cryostream monitored remotely using the software interface Cryopad[33] and by using a highly monochromatic wavelength (λ = 0.7107 Å). Images were processed using the software package CRYSALIS.[34] The structure was solved by direct methods (SHELXS-97),[35] which allowed the immediate location of the majority of the atoms composing the framework backbone. All the remaining non-hydrogen atoms were directly located from difference Fourier maps calculated from successive full-matrix least squares refinement cycles on F^2 using SHELXL-97.[36] All non-hydrogen atoms were successfully refined by using anisotropic displacement parameters. The last difference Fourier map synthesis showed the highest peak (1.121 e$Å^{-3}$) and deepest hole (−1.437 e$Å^{-3}$) located at 1.18 Å from Na(2) and 0.92 Å from Sm(1).

Very small, thin plates (average dimensions of $0.12\times0.04\times0.04$ mm) of Eu-AV-21, Tb-AV-21, and mixed-lanthanides Eu/Tb-AV-21, Eu/Gd-AV-21 and Tb/Gd-AV-21 were manually selected and mounted on a Hampton Research CryoLoops using FOMBLIN Y perfluoropolyether vacuum oil (LVAC 25/6) purchased from Aldrich[32] with the help of a Stemi 2000 stereomicroscope equipped with Carl Zeiss lenses. Data sets suitable for unit cell indexation were collected at 150(2) K on a Bruker X8 Kappa APEX II charge-coupled device (CCD) area-detector diffractometer ($Mo_{K\alpha}$ graphite-monochromated radiation, λ = 0.71073 Å) controlled by the APEX2 software package[37] and equipped with an Oxford Cryosystems Series 700 cryostream monitored remotely using the software interface Cryopad.[33] A full data set for La-AV-21 was collected with the same instrumental setup at 150(2) K up to a resolution of 0.60 Å. Systematic absences for this material were inspected using the software interface XPREP and ultimately the non-centrosymmetric *Cmm*2 space group was selected. Although other space groups seemed feasible (*C*222, *Cmmm*, and *Amm*2), the structure solution was not possible. The structure was solved by using Patterson methods implemented in SHELXS-97,[35] which allowed the location of the La and Si, with the remaining atoms being directly located from difference Fourier maps calculated from successive least-squares refinement cycles on F^2 using SHELXL.[30] All atoms were refined by assuming thermal anisotropic displacement parameters. Even though the hydrogen atoms associated with the water molecules of crystallization could not be located from difference Fourier maps, and no attempt was made to place these in calculated positions (due to the statistical disorder associated with these moieties), they have been included in the empirical formula of the compound. The last difference Fourier map synthesis showed the highest peak (2.429 e$Å^{-3}$) and deepest hole (−1.438 e$Å^{-3}$) located at 0.37 Å and 0.87 Å from Na(1), respectively.

Information concerning the crystallographic data collection and structure refinement details of Sm-AV-21 and La-AV-21 are summarized in Table 1. Selected bond lengths and angles for the Sm^{3+} and La^{3+} coordination environments are collected in Tables 2 and 4, respectively. Unit cell parameters for the members of the AV-21 system are given in Table 3.

Crystallographic information (excluding structure factors) for Sm-AV-21 and La-AV-21 can be obtained free of charge from Fachinformationszentrum Karlsruhe, 76344, Eggenstein-Leopoldshafen, Germany (e-mail: crysdata@fiz-karlsruhe.de), on quoting the depository numbers CSD-418915 and CSD-418916, respectively.

Powder X-ray diffraction (PXRD) patterns were collected on a X'Pert MPD Philips difractometer ($Cu_{K\alpha}$ radiation) with a curved graphite monochromator, a fixed divergence slit of 0.5°, and a flat plate sample holder, in a Bragg-Brentano para-focusing optics configuration. Analysis of the reported samples was performed with a step counting method (0.02° and

times between 5 and 10 s) in a range of 5–75° 2θ. LaB_6 was utilized as an internal PXRD peak position standard.

Through the utilization of an EDS Römteck System incorporated with a Hitachi S-4100 scanning electron microscope through a polymeric window, chemical analyses were rigorously performed.

Thermogravimetric (TGA) curves were measured with a Mettler TG50 Thermobalance. The samples were heated in a constant nitrogen flow at a rate of 5 °C/min from 25–750 °C. The thermally ejected 6.4 wt % and 6.6 wt % weight losses from Sm-AV-21 and La-AV-21 due to framework-occluded H_2O molecules correspond closely with the water content determined from the single-crystal X-ray analyses of 6.4 wt % and 6.8 wt %, respectively. Thermally activated H_2O desorption and subsequent resorption provided identical TGA curves and PXRD patterns consistent with stable microporous frameworks.

^{29}Si magic-angle spinning (MAS) NMR spectra of the Sm- and La-AV-21 frameworks were recorded at 79.49 MHz on a (9.4 T) Bruker Avance 400 wide-bore spectrometer, using 45° pulses, a 60 s recycle delay, and spinning rates of 5 or 15 kHz, respectively. Chemical shifts are quoted in parts per million from TMS.

The single-quantum ^{23}Na MAS NMR spectrum of Sm-AV-21 was measured with a recycle delay of 2 s using short powerful radio frequency pulses (15° pulse angle) and a fast spinning rate (15 kHz). The triple-quantum (3Q) ^{23}Na MAS NMR spectrum was recorded using the Z-filter three-pulse sequence. In this experiment, the excitation of the 3Q coherences and its conversion into 0Q coherences was achieved by applying two strong rf pulses, followed by a soft $\pi/2$ pulse (the so-called Z-filter). The symmetrization of pathways allows the simultaneous acquisition of the echo and anti-echo signals with equal intensity, leading to pure absorption spectra. The phase cycling was composed of six phases for the selection of 3Q coherences. This phase cycling was combined with a classic overall four-phase cycle to minimize phase and amplitude mis-settings of the receiver. The lengths of the first and second hard pulses were 3.80 and 1.32 μs, respectively. The length of the third soft pulse ($\nu_1 = 10$ kHz) was 12.5 μs. The MAS rate was $\nu_R = 15$ kHz. A total of 360 points were acquired in the t_1 domain in increments of $(1/2\nu_R) = 16.67$ μs. The recycle delay was 1 s, and 192 scans were recorded for each t_1 value. The ppm scale was referenced to the ν_o frequency in the ν_2 domain and to $3.78\nu_o$ in the ν_1 domain. Chemical shifts of all the ^{23}Na NMR spectra are quoted in ppm from a 1 M aqueous NaCl.

Room-temperature emission (PL), excitation (PLE), and lifetime measurements were recorded on a Fluorolog-3 (FL3–2T model) with a double excitation spectrometer, fitted with a 1200 grooves/nm grating blazed at 330 nm and a single emission spectrometer (TRIAX 320), fitted with a 1200 grooves/nm grating blazed at 500 nm, coupled to a R928P photomultiplier. The exciting sources were a 450 W Xe arc lamp and pulsed Xe-Hg lamps for the steady-state and time-resolved measurements, respectively. The excitation spectra (PLE) were corrected from 240–600 nm for the spectral distribution of the lamp intensity using a photodiode reference detector.

Acknowledgements

We are grateful to the Fundação para a Ciência e a Tecnologia (FCT, Portugal), FEDER, PTDC, and FAME NOE for the financial support. We also thank the ESRF (France, Grenoble) for allowing access to the Swiss-Norwegian BM01a beam line. C.M.K. thanks FCT for a Post Doctoral scholarship (SFRH/BPD/21039/2004).

[1] J. Rocha, M. W. Anderson, *Eur. J. Inorg. Chem.* **2000**, 801.
[2] R. Szostak, *Molecular Sieves*, Van Nostrand Reinhold, New York, **1989**.
[3] J. Rocha, L. D. Carlos, *Curr. Opinion Solid State Mater Sci.* **2003**, *7*, 199
[4] D. Ananias, A. Ferreira, J. Rocha, P. Ferreira, J. P. Rainho, C. Morais, L. D. Carlos, *J. Am. Chem. Soc.* **2001**, *123*, 5735.
[5] D. Ananias, M. Kostova, F. A. A. Paz, A. Ferreira, L. D. Carlos, J. Klinowski, J. Rocha, *J. Am. Chem. Soc.* **2004**, *126*, 10410.
[6] A. Ferreira, D. Ananias, L. D. Carlos, C. M. Morais, J. Rocha, *J. Am. Chem. Soc.* **2003**, *125*, 14573.
[7] M. H. Kostova, R. A. S. Ferreira, D. Ananias, L. D. Carlos, J. Rocha *J. Phys. Chem.* **2006**, *110*, 15312.
[8] D. Ananias, F. A. A. Paz, L. D. Carlos, F. G. C. Geraldes, J. Rocha, *Angew. Chem.* **2006**, *118*, 8106; *Angew. Chem. Int. Ed.* **2006**, *45*, 7938.
[9] G. M. Wang, J. Y. Li, J. H. Yu, P. Chen, Q. H. Pan, H. W. Song, R. R. Xu, *Chem. Mater.* **2006**, *18*, 5637.
[10] J. Rocha, L. D. Carlos, F. A. A. Paz, D. Ananias, J. Klinowski, *Proceedings: 14th International Zeolite Conference*, (Ed.: E. van Steen,) **2004**, Cape Town, South Africa, p. 3028.
[11] H.-K. Jeong, A. Chandrasekaran, M. Tsapatsis, *Chem. Commun.* **2002**, 2398.
[12] a) S. M. Haile, B. J. Wuensch, *Acta Crystallogr. Sect. A* **2000**, *56*, 335; b) S. M. Haile, B. J. Wuensch, *Acta Crystallogr. Sect. A* **2000**, *56*, 349.
[13] N. G. Shumyatskaya, A. A. Voronkov, Y. A. Pyatenko, *Kristallografiya* **1980**, *25* 728.
[14] a) M. D. McGehee, T. Bergstedt, C. Zhang, A. P. Saab, M. B. O'Regan, G. C. Bazan, V. I. Sardanov, A. J. Heeger, *Adv. Mater.* **1999**, *11*, 1349; b) G. F. Sá, O. L. Malta, C. Melo Donegá, A. M. Simas, R. L. Longo, P. A. Santa Cruz, E. F. Da Silva, Jr., *Coord. Chem. Rev.* **2000**, *196*, 165.
[15] a) *Lanthanide Probes in Life, Chemical and Earth Sciences, Theory and Practice* (Eds.: J. C. G. Bünzli, G. R. Choppin), Elsevier, Amsterdam, **1989**; Chapter 7; b) L. D. Carlos, Y. Messaddeq, H. F. Brito, R. A. S. Ferreira, V. de Zea Bermudez, S. J. L. Ribeiro, *Adv. Mater.* **2000**, *12*, 594.
[16] F. Cámaran L. Ottolini, B. Devouard, L. A. J. Garvie, H. C. Hawthorne, *Mineral. Mag.* **2006** ,*70*, 405.
[17] a) R. D. Shannon, *Acta Crystallogr. Sect. A* **1976**, *32*, 751–767; b) R. D. Shannon, C. T. Prewitt, *Acta Crystallogr. Sect. B* **1969**, *25*, 925–946.
[18] A. Sartbaeva, S. A. Wells, M. M. J. Treacy, M. F. Thorpe, *Nature Mater.* **2006**, *5*, 962.
[19] G. Wang, W. Yan, P. Chen, X. Wang, K. Qian, T. Su, J. Yu, *Micropor. Mesopor. Mater.* **2007**, *105*, 58.
[20] A. M. dos Santos, F. M. B. Marques, L. D. Carlos, J. Rocha, *J. Mater. Chem.* **2006**, *16*, 3139.
[21] D. L. Dexter, *J. Chem. Phys.* **1953**, *21*, 836.
[22] T. Förster, *Z. Naturforsch.* **1949**, *49*, 321.
[23] a) R. Evans, D. Ananias, D. Alastair; P. Douglas, L. D. Carlos, J. Rocha, *J. Phys. Chem. C*, 10.1021/jp0747104; b) R. Evans, L. D. Carlos, P. Douglas, J. Rocha, *J. Mater. Chem*. 10.1039/b715675h.
[24] H. P. You, X. Y. Wu, H. T. Cui, G. Y. Hong, *J. Lumin.* **2003**, *104*, 223.
[25] D. Sendor, M. Hilder, T. Juestel, P. C. Junk, U. H. Kynast, *New J. Chem.* **2003**, *27*, 1070.
[26] a) H.-Y. D. Ke, R. Birnbaum, *J. Lumin.* **1995**, *63*, 9; b) R. Reisfeld, C. K. Jørgenson, *Handbook on the Physics and Chemistry of Rare Earths, Vol. 9*, (Eds.: K. A. Gschneider, Jr., L. Eyring), Elsevier, Amsterdam, **1987**, pp. 61.
[27] M. F. Hazenkamp, G. Blasse *Chem. Mater.* **1990**, *2*, 105.
[28] a) D. L. Huber, *Phys. Rev. B* **1979**, *20*, 2307; b) D. L. Huber, *Phys.-Rev. B* **1979**, *20*, 5333.
[29] A. S. Gajadhar-Plummer, I. A. Kahwa, A. J. P. White, D. J. Williams *Inorg. Chem.* **1999**, *38*, 1745.
[30] I. A. Kahwa, C. C. Parkes, G. L. McPherson, *Phys. Rev.* **1995**, *52*, 11, 777.
[31] G. L. McPherson, Y. Y. Waguespack, T. C. Vanoy, W. J. Rodriguez, *J. Chem. Phys.* **1990**, *92*, 1768.
[32] T. Kottke, D. Stalke, *J. Appl. Crystallogr.* **1993**, *26*, 615–619.
[33] Cryopad, Remote monitoring and control, Version 1.451, Oxford Cryosystems, Oxford, (United Kingdom), **2006**.

[34] Oxford Diffraction, CRYSALIS Software Package, Version 1.171, Xcalibur Single Crystal CCD Diffractometer; Oxford Diffraction Sp.zo.o: Wroclaw, (Poland), **2001**; http://www.oxford-diffraction.com.
[35] G. M. Sheldrick, SHELXS-97, Program for Crystal Structure Solution, University of Göttingen (Germany), **1997**.
[36] G. M. Sheldrick, SHELXL-97, Program for Crystal Structure Refinement, University of Göttingen (Germany), **1997**.
[37] APEX2 Data Collection Software Version 2.1-RC13, Bruker AXS, Delft, (The Netherlands), **2006**.

Received: January 28, 2008
Revised: April 14, 2008
Published online: July 21, 2008

